Estimating Spectral Information of Complex Fenestration Systems in a Video-Goniophotometer

Eleanor C. Stokes, AB, Nicholas Gayeski, MSc, Marilyne Andersen*, PhD,

Building Technology Program, Department of Architecture, Massachusetts Institute of Technology, Cambridge MA, USA

short title: Spectral Estimation in a Video-Goniophotometer

* Corresponding author. Address for correspondence: M. Andersen, MIT Building 5-418, 77 Massachusetts Ave, Cambridge MA 02139, USA. Phone: 617-253-7714, Email: mand@mit.edu

Abstract

The effective use of complex fenestration systems in buildings requires knowledge of their optical spectral and directional properties. While the directional properties are commonly assessed by the measurement of bidirectional transmission or reflection distribution functions, the addition of spectral information would significantly aid in the design and analysis of such systems.

This paper describes the development of a spectral estimation method that reconstructs reflectance and transmittance spectra of unknown complex fenestration samples in the Heliodome, an innovative video-goniophotometer. The estimation method relies on the digital output of a tri-chromatic Charge-Coupled Device camera in eight filterbands to reconstruct a sample's spectrum using the truncated generalized singular value decomposition. This method is validated by comparing estimated spectra with documented reflectance and transmittance spectra of reference samples. In most spectrally selective materials, the method achieved average improvements of 50% over the Heliodome's previous quasi-spectral assessment method.

Nomenclature

BSDF	Bidirectional Scattering Distribution Function (sr^{-1})
$CS_\lambda(\theta_i,\phi_i,\theta_r,\phi_r)$	discrete conglomerate spectrum for designated incident and emerging angles ($\mu W/m^2$-sr)
d	digital response vector (components in units NDL/s)
$E_\lambda(\theta_i,\phi_i,\theta_r,\phi_r)$	discrete spectral bidirectional irradiance of initial polychromatic beam for the wavelength interval between 380nm and 945nm
f_1'	CIE (1987) measure of agreement between two spectra (percentage)
j (subscript)	filter combination number
k (as index)	truncation parameter (constant)
$L_\lambda(\theta_i,\phi_i,\theta_r,\phi_r)$	spectral bidirectional radiance in a polychromatic beam for the wavelength interval between 380nm and 945nm in discrete wavelength increments ($\mu W/m^2$-sr)
L_λ	spectral radiance viewed by the camera in discrete wavelength increments ($\mu W/m^2$-sr)
$L_{\lambda,j}$	spectral radiance viewed by the camera through filter j in discrete wavelength increments ($\mu W/m^2$-sr)
$M_{HMI,\lambda}$	spectral excitance of the HMI dedolight in discrete wavelength increments ($\mu W/m^2$)
n (index)	index identifying element in discretized vector

N	spectral modifier matrix (components in units NDL/s)
NDL_{RGB}	normalized digital level (digital level divided by 2^8) in the red, green, or blue channel
Q_f	flatness quotient defined in Eq. 16, where flatness is defined as having a $Q_f<0.1$
Q_s	smoothness quotient defined in Eq. 15, where smoothness is defined as having a $Q_s<0.1$
r_{RGB}	absolute spectral responsivity of CCD camera in the red, green, and blue channel (NDL/($\mu J/m^2$-sr))
S	second difference smoothing matrix
t_{int}	integration time for the camera (ms)
U	singular vectors resulting from SVD decomposition
V	vectors resulting from SVD decomposition
X	vectors resulting from GSVD decomposition
$\Delta\lambda_j$	wavelength interval corresponding to filterband j for quasi-spectral estimation
λ (subscript)	indicates a spectral distribution of a radiometric quantity recorded in discrete wavelength increments
ε	random error vector (NDL/s)
μ	denominator of singular values in GSVD
ϕ_i	incident azimuth angle (radians)
ϕ_r	reflected azimuth angle (radians)

$\bar{\rho}$	estimated spectral reflectance or transmittance with error component in d
ρ_{box}	average reflectance or transmittance for each waveband determined by the camera's filtered radiance predictions
ρ_{k}	estimated spectral reflectance or transmittance using TSVD, truncating at k singular values
ρ_{reg}	an estimated spectral reflectance or transmittance using regulation methods
ρ_{sample}	measured spectral reflectance or transmittance for the sample
$\rho_{spheroid}(\theta_i,\phi_i,\theta_r,\phi_r)$	bidirectional spectral reflectance of the spheroid
$\varnothing$	singular values in SVD, and numerator of singular values in GSVD
$\tau_{spheroid}(\theta_i,\phi_i,\theta_r,\phi_r)$	bidirectional spectral transmittance of the spheroid
θ_i	incident altitude angle (radians)
θ_r	reflected alititude angle (radians)

Introduction

The benefits of thoughtful daylighting in buildings range from aesthetically pleasing spaces to energy conservation, to improved visual comfort or even a sense of well-being. Over the past decades, complex fenestration systems (CFS) have improved the ability to control light collection and redistribution, increasing the amount of “useful” daylight, or daylight that aids in visual tasks and illuminates a space without discomfort.

The development of CFS requires a thorough investigation of the directional and spectral modifications of a light beam after it has been reflected off or transmitted through a glazing sample. The directional component of the beam can be expressed as a four variable function called a BSDF (Bidirectional Scattering Distribution Function). Each of the variables represents an incident or emerging angle, which describes the distribution of light before and after it hits a fenestration sample. BSDFs are used in a broad range of fields, from computer rendering to texture studies to luminaire characterization. The tool designed to measure these functions is called a bidirectional goniophotometer.

There have been several iterations of such goniophotometers designed specifically to study daylighting on fenestration materials. An overview of the existing models is outlined in Andersen[1]. Most of the mentioned goniophotometers use a scanning method, where a detector gathers BSDF

information at a series of predetermined points forming a hemisphere around the sample. This technique is both time intensive and discrete, risking missed narrow spikes in areas between measurement points. However, speedier approaches have been developed using a Charge-Coupled Device (CCD) camera to detect the distribution of light from all emerging angles simultaneously [2,3].

The MIT Heliodome, an innovative video-goniophotometer covering both the visible and the Near-Infrared ranges, has been developed using this camera approach. The goniophotometer uses a semi-transparent mirrored hemispheroid[3] to redirect the emerging light from the sample to the camera's lens, quickly capturing the full light distribution for each incident angle. The Heliodome also provides both photometric functions, and spectral information across the visible and NIR regions of the solar spectrum. Together, these innovations make the Heliodome important for the design and analysis of CFS and their effective use of daylighting in a space.

This paper concentrates on the most recent step in the Helidome's progress - the development of a method to estimate the reflection and transmission spectra of fenestration system materials based on the camera-evaluated colour coordinates of the emerging filtered light.

Previously, many glazing technologies and shading systems have been evaluated solely on their thermal properties, neglecting their effect on the Correlated Colour Temperature (CCT) and colour-rendering index (CRI) of incoming light. As described in Chain[4], often this neglect leads to lowered visual performance, negative impact on the environment, and little control over the colour appearance of the space. Understanding the spectral power distribution (SPD) of emerging light is integral for control over the colour surfaces and visual satisfaction of the occupants.

Spectral information is also used to control solar gains in spectrally selective glazings. These glazings are designed to allow maximal visible light transmission, while seasonally controlling NIR transmission to lessen HVAC loads. Through the application of a minimally emissive coating, spectrally selective glazings reduce solar heat gains in summer and heat loss in the winter. The benefits of these selective coatings include increased transparency over tinted glass, downsizing mechanical heating and cooling systems, and cost paybacks in 3-10 years[5]. However, by combining fenestration light distribution techniques with spectral modification techniques, systems could be designed that handle the heat of light differently from the visible component. This combination has profound implications on thermal glare mitigation and the efficient use of thermal masses.

Furthermore, though quasi-spectral radiometric measurements provide a general idea about radiation distribution in a space, a gross approximation to spectral information is inadequate for multi-layered systems. When fenestration materials are layered, their reflectance or transmittance spectra cannot be averaged over large bands, but instead must be multiplied wavelength by wavelength. Thus, an optimal result requires detailed knowledge of the spectral information of each layer in an assembly.

2. State of the Art

2.1 Spectral Goniophotometers

The incorporation of spectral characterization into goniophotometry for daylighting applications was first proposed by Breitenbach and Rosenfeld at Cardiff University, UK[6]. The Cardiff instrument, now at the Technical University of Denmark (DTU), utilizes two scanning spectrometers attached to an off axis parabolic mirror used for light collection. Another goniophotometer, designed by the consultancy company *pab-opto*[7], uses a variety of light sources and a modular detector concept that can be adapted to different applications. The choice of detectors cover radiometric, photometric, IR, and multi-channel spectral ranges to give quasi-spectral BSDF measurements.

While these few existing goniophotometers already collect spectral information, none currently use cameras to measure reflectance and

transmittance spectra. Most existing methods involving spectroradiometers and tunable monochromators are expensive and time inefficient[8]. The Heliodome's camera-based procedure provides this spectral information much faster, enabling an easier complete characterization of CFSs.

2.2 Spectral Estimation Methods

As an alternative to traditional spectroradiometers, spectral estimation methods using digital imaging have been examined in detail. These methods aim to provide the SPD associated with each pixel in a scene captured by a digital camera through the use of computational image-processing algorithms. Many of the methods modify the standard assumption of low dimensional linear models in order to estimate spectra for a variety of applications[9,10,11,13].

The technique used for most spectral reflectance estimation is based on the principal component analysis of low dimensional linear models. Studies have shown that this technique is adequate for reconstructions of natural illuminants and situations with known camera properties[8,11,14,15]. Spectral estimation in the Helidome combines this a priori method with other regularization techniques to design an appropriate routine for the spectral reflection and transmission reconstruction of CFS in a goniophotometer.

3. Helidome Design Concept

The Heliodome is automated for both the visualization of sunlight distribution inside a scale model, and the measurement of video-based BSDFs of materials. Much work has been completed on the Heliodome's mechanical design, lighting components, and camera calibrations, and is described in [16] and [17]. Its functioning principle and major components are outlined here to familiarize the reader with concepts assumed in the spectral estimation method.

The Heliodome was modeled after a prototype designed for computer graphics applications,[3] using a mirrored hemisphere as a projection screen which would reflect light emerging from the sample into a CCD camera detector. This design was modified so the mirrored surface is semi-transparent, allowing transmission measurements in addition to reflection measurements. Also, the hemisphere was changed to a hemi-spheroid in order to create two focal points—one where the camera is positioned, and the other at the position of the fenestration sample.

A HMI collimated light source filtered into broadband sections illuminates the sample which then transmits (or reflects) the emerging distribution onto the hemi-spheroid. As shown in Figure 1, due to the geometry of the hemi-

spheroid, all emerging light will travel from one focal point to the other focal point, onto the fish-eye lens of the camera.

Figure 1

When the radiation reaches the camera, the resulting image is spatially calibrated so that each pixel corresponds to a small area on the hemi-spheroid. The camera is also calibrated to act as a radiometer as described in[16]. Images are taken at different exposure levels to create a High Dynamic Range (HDR) image[18] for each of eight filter combinations (numbered with subscript j=1 to 8 in this paper). These eight HDR images map the entire emerging distribution of light (one BTDF or BRDF) for the chosen incident beam angle.

Before their combination into eight HDR images, the same pixel in each of the raw filterband images is analyzed at several exposure times to give a radiance step curve. Each step describes the radiance of the beam in a particular waveband $\Delta\lambda_j$ (with j=1 to 8 corresponding to each of the eight filtersets), which has been reflected from the corresponding location on the hemi-spheroid. While the filters are not box-like, the waveband is a close approximation to the actual filter transmittance, achieving estimations within 10% of the true radiance in each $\Delta\lambda_j$ [16]. The radiance step curve can be changed into a quasi-spectral step curve, ρ_{box}, describing a rough spectral

transmittance or reflectance estimation of the sample. The goal of the spectral estimation method is to get finer knowledge of the spectral aspects of samples, gaining an improvement over $\rho_{box.}$

This quasi-spectral angular distribution can be evaluated over both the visible and NIR portions of the solar spectrum. The two cameras, a CCD camera for the 380-945nm range and an InGaAs camera for the 900nm-1700nm range, use sensors to associate the radiation impinging on the camera's lens with a corresponding pixel value. Because the CCD camera uses three sensors (red, green, and blue) and the NIR camera only uses one, and because fine spectral modifications in the visible radiation are of great interest, the following discussion will focus on the use of the CCD camera.

4. Spectral Estimation Method for Unknown Spectra

4.1 Experimental Constraint

To derive the reflection or transmission coefficients of a fenestration sample, the Heliodome's measurement process must be described mathematically. The two modes differ only in that, for reflectance measurements, the incident beam must be initially transmitted through the spheroid before reaching the sample. The spectral estimation of transmittance spectra can be seen as a

specific subcase ($\tau_{spheroid}$=1 for all λ) of the general spectral reflectance estimation method. Therefore, this paper will describe the methodology in reflection mode, starting with the deliverable - the series of filtered images taken by the camera.

4.1.1 Deriving the camera digital response vector

The digital output of the colour CCD camera for each filter, $NDL_{RGB,\,j}$, is related to the radiance seen by the camera $L_{j,\lambda}$ by a logistic dose response function, f, described in [16]:

$$NDL_{RGB,\,j}=f(\,t_{int,j}\,\Sigma_{\lambda}L_{j,\lambda}r_{RGB,\lambda}) \qquad (4)$$

where j= [1,8] and λ=[380,945] in 5 nm increments. $r_{RGB,\lambda}$ is the CCD camera's absolute spectral responsivity (ASR) and $t_{int,j}$ is the integration time of the image. To isolate the reflection coefficients of the sample, the expression linking NDL to $L_{j,\lambda}$ must be further dissected:

$$f^{-1}(\,NDL_{RGB,j})/\,t_{int,j}=r_{RGB,\lambda}\circ L_{j,\lambda} \qquad (5)$$

The dot product, $f^{-1}(\,NDL_{RGB,j})/\,t_{int,j}$, can be compiled into a vector of length 24, called d:

$$d=\begin{bmatrix} f^{-1}(NDL_{R,1})/t_{int,1} \\ f^{-1}(NDL_{G,1})/t_{int,1} \\ f^{-1}(NDL_{B,1})/t_{int,1} \\ \vdots \\ f^{-1}(NDL_{B,8})/t_{int,8} \end{bmatrix}$$

Everything in d is known from the camera's image and camera settings.

4.1.2 Deriving the spectral modifier matrix

The other side of the expression contains the unknown spectral radiance of the beam reaching the fisheye, $L_{j,\lambda.}$ To isolate the reflection coefficients of the unknown sample, $L_{j,\lambda}$ is represented as a product of its contributing parts. Each spectrum can be seen in Figure 2, and affect the relative spectrum of the initial beam in different ways depending on their flatness.

Figure 2

The reflectance and transmittance spectra of the spheroid, based on experimental results[16], vary for each pixel depending on variations in the reflective coating. On account of this and other geometrical imperfections, another hemispheroid is being manufactured for the finalized Helidome. In this paper, the spectral estimation method will therefore be described for a single pixel corresponding to angle $(\theta_i,\phi_i,\theta_r,\phi_r)$.

The initial spectral exitance of the beam, $M_{HMI,\lambda}$, is modified as shown below:

$$L_{j,\lambda}(\theta_i,\phi_i,\theta_r,\phi_r)=M_{HMI,\lambda}\cdot{}^{*}\tau_{filter,j,\lambda}{}^{*}\tau_{spheroid,\lambda}(\theta_i,\phi_i)\cdot{}^{*}\rho_{sample,\lambda}(\theta_i,\phi_i,\theta_r,\phi_r)\cdot{}^{*}\rho_{spheroid,\lambda}(\theta_r,\phi_r) \quad (6)$$

where

$\tau_{filter,j,\lambda}$ is the transmission spectrum of filter j

$\tau_{spheroid,\lambda}$ (θ_i,ϕ_i) is the transmission spectrum of the spheroid for an incident altitude and azimuth angle (θ_i,ϕ_i)

$\rho_{sample,\lambda}$ $(\theta_i,\phi_i,\theta_r,\phi_r)$ is the reflection spectrum of the unknown sample along emerging direction (θ_r,ϕ_r) from a beam of incident angle (θ_i,ϕ_i)

$\rho_{spheroid,\lambda}$ (θ_r,ϕ_r) is the reflection spectrum of the spheroid corresponding to the angle (θ_r,ϕ_r)

all recorded in 5 nm wavelength increments. The symbol $\cdot*$ is the scalar multiplication of the elements in corresponding vector row indices.

Combining the known components of the spectrum yields:

$$CS_{j,\lambda}(\theta_i,\phi_i,\theta_r,\phi_r) = [M_{HMI,\lambda} \cdot * \tau_{filter,j,\lambda} \cdot * \tau_{spheroid,\lambda}(\theta_i,\phi_i) \cdot * \rho_{spheroid,\lambda}(\theta_r,\phi_r)] \quad (7)$$

where $CS_{j,\lambda}$ is the conglomerate spectrum for filterset j, or discrete spectral radiance as viewed by the camera as if there were no sample. Transforming the dot product, Eqn 5 becomes:

$$f^{-1}(NDL_{RGB,j})/t_{int,j} = r_{RGB,\lambda}[CS_{j,\lambda}(\theta_i,\phi_i,\theta_r,\phi_r)]^T[\rho_{sample,\lambda}(\theta_i,\phi_i,\theta_r,\phi_r)] \quad (8)$$

The row vectors, $r_{RGB,\lambda}[CS_{j,\lambda}(\theta_i,\phi_i,\theta_r,\phi_r)]^T$, are combined in a matrix N corresponding with vector d:

$$N(\theta_i,\phi_i,\theta_r,\phi_r) = \begin{bmatrix} r_{R,\lambda}CS_{1,\lambda}(\theta_i,\phi_i,\theta_r,\phi_r)^T \\ r_{G,\lambda}CS_{1,\lambda}(\theta_i,\phi_i,\theta_r,\phi_r)^T \\ r_{B,\lambda}CS_{1,\lambda}(\theta_i,\phi_i,\theta_r,\phi_r)^T \\ \vdots \\ r_{B,\lambda}CS_{8,\lambda}(\theta_i,\phi_i,\theta_r,\phi_r)^T \end{bmatrix}$$

If ρ_{sample} is measured at 5nm intervals, the final expression:

$$N\rho_{sample}=d \quad (9)$$

is a linear system with 24 equations (8 filters x 3 colour channels) and 114 unknown reflection coefficients.

The intuitive solution to this matrix expression would be to use the pseudoinverse of N to solve for ρ_{sample}:

$$N^{+}=(N^{T}N)^{-1}N^{T} \quad (10)$$

$$\rho_{sample}= N^{+}d \quad (11)$$

If N were a full rank matrix, requiring thirty-eight filters, and d were a perfectly calibrated sampling of digital responses from the camera, the pseudoinverse solution would be a perfect match. However as the pseudoinverse is highly sensitive to noise and error[19,20], alone it is not a practical solution for our application.

Since the system is ill-posed, there are many metamers that satisfy Eqn 9, i.e. many different spectral power distributions that would still correspond to the same combination of R, G and B values. Additional information is needed to weed out these metamers and find the vector that most reasonably estimates a probable ρ_{sample} .

4.2 Smoothness Constraint

To further constrain the problem, the solution, ρ_{reg}, approximating ρ_{sample}, can be assumed to be a smooth reflectance curve, a condition similarly used in Li-Luo[21] and van Trigt[22]. Severe monochromatic-like peaks are very unlikely to occur in the reflectance or transmittance spectra of fenestration, so the assumption of smoothness is not overly restrictive for our purposes. As a result of this assumption, each consecutive element of the vector ρ_{reg} cannot differ dramatically from the next. Thus, we use a second difference matrix S, curtailed to address the boundary conditions:

$$S = \begin{bmatrix} 1 & -2 & 1 & 0 & 0 & 0 & \dots \\ 0 & 1 & -2 & 1 & 0 & 0 & \\ 0 & 0 & 1 & -2 & 1 & 0 & \\ \vdots & & & & & & \\ 0 & 0 & 0 & 1 & -2 & 1 & \end{bmatrix}$$

A smooth choice for ρ_{reg} requires the minimization of the second norm $||S\rho_{reg}||_2$.

4.3 Regulation Methods

The problem to be solved is one of balancing these two criteria correctly. Though there will be expected errors in the radiance estimates, ρ_{reg} must still closely satisfy the linear system, minimizing $||N\rho_{reg} - d||_2$. Additionally, solutions with dramatic perturbations over small wavebands must also be eliminated by

minimizing the side constraint, $||S\rho_{reg}||_2$. A ρ_{reg} is chosen that balances these two concerns such that ρ_{reg} is reasonably close to the unknown solution ρ_{sample}. While ρ_{reg} is not constrained such that all its coefficients are less than one, satisfying the linear system requires that energy be conserved, so the system would only violate this restriction if radiance values implied an almost completely transmissive or reflective sample.

This solution could be found using many regularization methods[23]. For truncated generalized singular value decomposition (TGSVD)[24,25], the method chosen for the Helidome's application, the solution is:

$$\rho_k = \sum_{n=112-k+1}^{112} \frac{u_n^T d\ x_n}{ø_n} + \sum_{n=113}^{114} u_n^T d\ x_n \qquad (12)$$

where ρ_k is the reflectance spectra estimated using the first k singular values of N, and x_n is the n^{th} vector of matrix X from the generalized singular value decomposition.[24,25].

5. Theoretical validation of the spectral estimation method assuming errors in d

5.1 L-curve Analysis

It is vital that the camera calibration be as accurate as possible, since the response from the camera in all three channels is the link between ρ_k and ρ_{sample}. However, due to the limits on radiometric accuracy that non-theoretical filters[16] impose on the NDL measurements, the spectral estimation method must plan for error contributions to the vector d.

These errors create a perturbed $\bar{d}$, from which $\bar{\rho}_k$ must be inferred. Figure 3 shows a comparison of ρ_k from d, with the best manually chosen $\bar{\rho}_k$ from $\bar{d}$, the same vector with added randomly distributed noise. In these hypothetical examples, when $\bar{\rho}_k$ is optimally truncated, it converges towards ρ_k. The question is, then, how to choose k optimally.

Figure 3

It is useful to identify the types of error introduced into the approximated solution. The first of these errors is associated with the camera's calibration, and can be written as the difference:

$$\bar{d} - d = \varepsilon \qquad (13)$$

where d is the unperturbed vector and where ε is a random error component. The second of these comprises the errors inherent in the regularization approximation.

A graphical tool called an L-curve[27,28], plots the semi-norm of both contributions. With an L-curve, one can find the minimization point, where $\bar{\rho}_k$ should be least affected. When plotted on a log-log scale, these graphs have a characteristic L-shape, where the corner marks the minimization point. Here, the vertical component (contributions from $||S\ \bar{\rho}_k||$) meets the horizontal component (contributions from $||N\ \bar{\rho}_k - d||$).

5.2 **Error analysis results**

As is demonstrated in the series of truncations for the coated sample shown in Figure 4, as k increases and $ø_n$ decreases, and the estimation $\bar{\rho}_k$ of this sample begins to fluctuate more noticeably. This is due to the contribution of the perturbation error ε for small singular values. However, when k is too low, the regulation error is high and $||N\ \bar{\rho}_k - d||$ does not adequately approximate ρ_k. Thus, the L-curve for this sample, shown in Figure 5, is used to determine the appropriate value for k, in this case k=9, so as to get an optimal $\bar{\rho}_k$ for the given sample.

Figure 4-6

When compared with ρ_{box} these truncations achieve significantly closer approximations to ρ_{sample}. By averaging the distances:

$$||(\rho_{box} - \rho_{sample})||_2 \quad \text{and} \quad ||(\bar{\rho}_k - \rho_{sample})||_2 \tag{14}$$

one can calculate the percentage of error reduction of $\bar{\rho}_k$ over ρ_{box}. For the coating sample shown in Figure 6, this error was reduced by 94%, for the chosen $\bar{\rho}_k$ approximation. Such high error reductions can commonly be achieved for samples that rapidly vary within a given waveband, as in the 650-850nm waveband for the given example.

While this sample varies rapidly, it is important to note that a less variant metamer would never be a satisfactory solution. One could imagine a metamer spectrum peaking around 650nm that may better satisfy the smoothness criteria, however, this metamer would also have to maintain a minimum $||N\ \bar{\rho}_k - d||$, requiring close approximations to the step curve in every waveband. Thus, the only acceptable metamers under this system would be those unintentionally fostered by camera error, with less variant spectral portions *within* complementary wavebands.

An error analysis was performed for 48 reflectance and transmittance spectra chosen from four fenestration categories documented in the Optics 5 database. In each case, the improvement of $\bar{\rho}_k$ over ρ_{box} was calculated, along with a smoothness quotient:

$$Q_s = \sum_{n=2}^{112} \left| \left(\rho_{sample,\lambda,n+1} + \rho_{sample,\lambda,n-1} \right) - 2\rho_{sample,\lambda,n} \right| \quad \text{with} \quad \rho_{sample,\lambda,n} \in \rho_{sample,\lambda} \quad (15)$$

and a flatness quotient:

$$Q_f = | \min(\rho_{sample,\lambda}) - \max(\rho_{sample,\lambda}) | \quad (16)$$

Smooth or flat samples were defined as having respective quotients less than 0.1. To quantify the agreement between $\bar{\rho}_k$ with ρ_{sample}, independent of ρ_{box}, the function f_1' (CIE (1987)) was also calculated for each spectral estimation.

The average improvement of $\bar{\rho}_k$ over ρ_{box} for all 48 spectra was 58%; 51% for reflectance spectra and 73% improvement for transmittance spectra. For the same samples, the average f_1' was 9.4%. Broken up by glazing type, the average improvements were 69% for the applied films, 75% for coatings, 50% for monolithic samples, and 37% for laminates. This equated to a f_1' of 9.8% for applied films, 8.7% for coatings, 9.1% for monolithic samples, and 16.7% for laminates. Greater improvements are mostly due to differences in smoothness and variance. The tested applied films in particular, such as Solis and Solarguard coloured films, had less smooth reflectance and transmission spectra, with an average quotient of 0.6 compared to quotients around 0.3 for the other three categories. In fact, when categorizing the samples according to these spectral properties, fluctuating spectra achieved an average improvement of 68%, compared to only 35% for samples with smooth spectra. Also variant spectra achieved an average improvement of 70% compared to 32% for samples with flat spectra.

It should be noted that smaller reductions in error are not indications of poor spectral fits, but instead may indicate that ρ_{box} was initially a closer estimate to ρ_{sample}. The f_1' for smooth samples (6.8%), for example, was actually lower than for fluctuating samples (15.9%) , though the relative improvement was greater for fluctuating samples. For example, for the reflectance spectrum shown in Figure 8, the sample yielding the lowest percent error reduction, a dark grey laminate, was essentially constant.

Figure 8

6. Experimental validation using spectrally selective samples

The spectral estimation method was also validated by the use of nine spectrally selective samples gathered from a variety of fenestration material manufacturers. The materials were a mixture of applied film samples, coated glasses, and laminate configurations and were assumed to be generally representative of the larger body of glazing materials used in complex fenestration systems.

By performing the validation with real samples, actual images from the Kappa colour CCD camera calibrated for the Heliodome[16] could be used. To isolate the spectral estimation method and examine its soundness apart from the other components of the Heliodome, this experimental validation was realized without the spheroid, whose geometry and coating characteristics are still

being improved. Also, since transmitted light can be measured more easily and accurately than reflected light, these samples were analyzed in transmission mode only for this validation exercise, but the results are equally applicable to both modes.

As shown in Figure 9a, a USB2000 spectrometer was used to measure each sample's spectral transmission coefficients across the 380 to 900nm range. The emittance spectrum of a tungsten lamp as source was compared before and after transmission through the sample. The spectrometer was also used in conjunction with the filters to find the absolute spectral power distribution (SPD) of the beam after it has been transmitted through each filter and the unknown sample. The integral of these SPDs is the true radiance in each waveband.

The sample's now known (measured) transmission spectrum could then be compared with the spectrum predicted when the camera's digital levels were used as inputs into the spectral estimation method for a series of images taken at different exposures in each filterband.

Figure 9

The camera was set-up facing a Spectralon coated diffusing reflectance standard positioned behind the unknown sample, as shown in Figure 9b. For

each filter, images were taken of the standard at exposure times ranging from first detection to pixel saturation. The digital levels registered by the most sensitive “best” channel were then linked to a total radiance estimate for each filter interval. When compared with the spectrometer measurements, these estimates were within 10% of the true radiance. The total radiance estimates for each filter interval are directly related to the rough step function, ρ_{box}.

One advantage of the spectral estimation method over this rough step function is its use of all the registering channels in each filter interval, instead of only the prescribed “best” channel. This allows the spectral reflectance or transmittance curve to be further refined other channels yielding reasonably close radiance estimates.

Among the nine tested samples, the spectral estimation method achieved an average improvement of 54% over the quasi-spectral estimation, ρ_{box}. Similarly to what was observed with hypothetical samples, flat transmission spectra had the lowest relative improvement at 35.3%, such as for sample H-8.3, a monolithic clear fenestration material. Also, as shown in Figure 10, the smooth, yet variant, coated sample C4 gains a 71% improvement over ρ_{box}. Unlike the hypothetical sample tests, considering the large error component from the camera, the method should achieve lower average distances between $\bar{\rho}_k$ and ρ_{sample} for smooth samples. This error component forces the method to

truncate the estimation early, at k=2. With fewer singular values, the method more easily estimates spectra with fluid transmission and reflection spectra. As most fenestration materials do not aspire to sharp spectral shifts, this tendency is generally benign.

Figure 10

General trends in relative improvement, however, are harder to predict for real samples, since *both* ρ_k and ρ_{box} now contain an error component, unlike the ρ_{box} estimations discussed in section 7. As shown in Figure 10, even nearly flat samples can achieve 70% improvements. In this case the improvement is high because of the inaccuracy of ρ_{box}. For flat samples, a smooth ρ_k easily results in grand improvements if the 10% error contribution from the camera manifests itself in alternating over and under-predictions for each waveband of ρ_{box}.

Figure 11

7. Estimating BSDFs for spectrally selective samples

The spectral estimation method fits into the larger context of the Heliodome, by providing the spectral information needed to supplement a spectral radiometric BSDFs. For each pixel, the spectrum estimation method will be applied, resulting in a reflectance or transmittance spectra for the sample, ρ_k, correlated to every incident and emerging direction pair. By substituting this known ρ_k for

the unknown ρ_{sample} in an unfiltered version of Eq. 6, the quantity L_λ can be calculated for every pixel for images taken at a chosen incident angle. Depending on the angular resolution of the spatial calibration, the discrete spectral radiance $L_\lambda(\theta_i,\phi_i,\theta_r,\phi_r)$ can be averaged, element by element, over chosen solid units of angle.

The irradiance on the sample, $E_\lambda(\theta_i,\phi_i)$, for each incident angle (θ_i,ϕ_i), can be calculated from aforementioned known quantities:

$$E_\lambda(\theta_i,\phi_i) = M_{HMI,\lambda} * \tau_{spheroid,\lambda}(\theta_i,\phi_i) \cdot * \cos(\theta_i) \qquad (18)$$

where

$\tau_{spheroid,\lambda}(\theta_i,\phi_i)$ is the discrete transmission spectrum of the spheroid at incident angle (θ_i,ϕ_i)

$M_{HMI,\lambda}$ is the discrete spectral excitance of the HMI beam

and $\cos(\theta_i)$ accounts for the effect of off-normal radiation

Finally, these two quantities can be used to calculate spectral BSDFs. Spectral radiometric BSDFs are defined as the ratio of radiance $L(\theta_i,\phi_i,\theta_r,\phi_r)$ and irradiance $E(\theta_i,\phi_i)$ and can be expressed in a partial derivative form by the following equation:

$$BSDF_\lambda(\theta_i,\phi_i,\theta_r,\phi_r) = \frac{L_\lambda(\theta_i,\phi_i,\theta_r,\phi_r)}{E_\lambda(\theta_i,\phi_i)} \qquad (17)$$

The result will describe how a sample spectrally modifies and distributes incident light throughout a space. One can see how this kind of detailed characterization can foster imaginative fenestration design. For example, incident light from different seasonal angles could be reorganized according to its spectral distribution--the NIR component in one direction (e.g. to a thermal mass) and the visible component in another direction (onto a reflective surface). Certainly, a better understanding of the complete BSDF *and* the directional reflectance or transmittance of complex fenestration systems will offer the possibility for greater control of solar radiation.

10. Conclusion

In this paper, a spectrum estimation method has been developed for the MIT Heliodome. Using the digital response of a CCD camera and the known spectral modifications to incident light of each component in the Heliodome system, the spectral reflectance or transmittance spectra of an unknown sample can be derived. The sample's spectrum is approximated by TGSVD, and the errors are analyzed to choose the correct point of truncation. A resulting spectrum can be associated with each pixel in a CCD image, such that a complete spectral BSDF for the sample can be constructed for every incident and emerging direction pair.

The spectral estimation method was successful for the hypothetical and for the real samples tested. The method has been validated, showing average improvements of 70% in the estimation of spectral reflectance and transmittance for highly spectrally selective reference samples, and 40% for samples with flatter and smoother reflectance or transmittance spectra. In the experimental validation, these improvements averaged 50%.

This method completes spectral characterization of distributed light and will facilitate the intelligent design of future complex fenestration systems. Useful especially for multi-layered CFS design, the spectral characterization of each component could clarify the overall spectral reflectance and transmittance of the system. Since component spectra are multiplied on a wavelength by wavelength basis, average or non-spectral reflectance and transmission coefficients would be ill-suited to describe the effectiveness of the system as a whole.

Additionally, spectral information as it is related to a directional distribution of solar radiation and visible light is especially relevant in the design of passive heating and lighting strategies. The combination of directional and spectral information opens up new options for optimal design tactics, and deserves to become more readily accessible as complex fenestration systems become integrated into new simulation software. In hopes of addressing these

informational voids, the spectral estimation method will be integrated into the Heliodome in its final form upon completion of the manufacture of a new spheroid.

Acknowledgements

This work was jointly supported by the Massachusetts Institute of Technology and by the National Science Foundation under Grant No. 0533269. The authors wish to thank Michael Rubin for providing us information and samples of spectrally selective materials, Tanury Industries and Spartech Corporation for their generous efforts in producing the first hemi-spheroids and Replex Plastics for their creativity in making new ones. They also wish to acknowledge Courtney Phillips and undergraduate students Dean Ljubicic, Zachary Clifford, Timothy Koch, Jason Ku, Keith Molina, Javier Burgos, Samuel Kronick and Danh Vo for their contributions to the device.

REFERENCES

[1]Andersen M, Michel L, Roecker C, Scartezzini JL. Experimental assessment of bi-directional transmission distribution functions using digital imaging techniques. *Energy and Buildings* 2001; 33: 417-431.

[2]Andersen M, Rubin M, Powles R, Scartezzini JL. Design of a time-efficient video-goniophotometer combining bidirectional functions assessment for

transmission and reflection. *Solar Energy Materials and Solar Cells* 2005; 88: 97-118.

[3]Ward G. Measuring and Modeling Anistropic Reflection. *Computer Graphics* 1992; 26: 265-272.

[4]Chain C, Dumortier D, Fontoynont M. Consideration of Daylight's color. *Energy and Buildings* 2001; 22: 193-198.

[5]Pacific Northwest National Laboratory. *Spectrally Selective Glazings*. U.S. Department of Energy, DOE/EE-0173, Berkeley, August 1998.

[6]Breitenbach J, Rosenfeld JLJ. Goniospectrometer measurements of the optical performance of a holographic optical element. *Solar Energy* 2000; 68: 427-437.

[7]Apian-Bennewitz P. *pab Goniophotometer II*. Retrieved 20 Nov 2007, from http://www.pab-opto.de/gonio-photometer/

[8]Nieves JL, Valero EM, Hernandez-Andres J, Romero J. Recovering fluorescent spectra with a n RGB digital camera and color filters using different matrix factorizations. *Applied Optics* 2007; 46: 4144-4154.

[9]Maloney LT, Wandell BA, Color constancy: a method for recovering surface spectral reflectance. *J. Opt. Soc. Am* 1986; A 3: 29-33.

[10]Connah D, Westland S, Thomson MGA, Recovering spectral information using digital camera systems. *Color Technology* 2001; 117: 309-312.

[11]Hernandez-Andres J, Nieves JL, Valero EM, Romero J. Spectral-daylight recovery by use of only a few sensors. *J. Opt. Soc. Am.* 2004; A 21: 13-23.

[12]Imai FH, Berns RS. *Spectral estimation using trichromatic digital cameras. Proceedings of the International Symposium on Multipectral Imaging and Color Reproduction for Digital Archives*, Society of Multispectral Imaging of Japan,1999.

[13]Cheung V, Westland S, Li C, Hardeberg J, Connah D, Characterization of trichromatic color cameras by using a new multispectral imaging technique. *J. Opt. Soc. Am*. 2005; A 7: 1231-1240.

[14]Romero J, Garcia-Beltran A, Hernandez-Andres J, Linear bases for representation of natural and artificial illuminants. *J. Opt. Soc. Am*. 1997; A 14: 1007-1014.

[15]Maloney LT, Evaluation of linear models of surface spectral reflectance with small numbers of parameters. *J. Opt. Sco. Am*. 1986; A 3: 1673-1683.

[16]Gayeski N, Andersen M. *New Methods for Assessing Spectral, Bi-directional Transmission and Reflection by Complex Fenestration Systems. Proceedings*

of SOLAR 2007: Sustainable Energy Puts America to Work. Cleveland. 7-10 July 2007.

[17]Andersen M, Gayeski N, Stokes E, Osser R, Browne C. *The Heliodome project: an innovative approach in assessing solar-optical properties of light-redirecting materials in combination with sun course simulations. Proceedings CISBAT 2007: Renewables in a changing climate - Innovation in the Built Environment*; Lausanne. 4-5 September 2007.

[18]Inanici MN. Evaluation of high dynamic range photography as a luminance data acquisition system. *Lighting Research & Technology* 2006; 38: 1-14.

[19]Neumaier A. Solving ill-conditioned and singular linear systems: A tutorial on regularization. *SIAM Review* 1998; 40: 636-666.

[20]Hardeberg JY. *Acquisition and reproduction of colour images: colorimetric and multispectral approaches*. Ph.D. thesis. Ecole Nationale Superieure des Telecommunicationes, Paris,1999.

[21]Li CJ, Luo MR. *The estimation of spectral reflectances using the smoothness constraint condition. Proceeding of the 9th Color Imaging Science Conference*. Springfield: Society for Imaging Science and Technology, 2001.

[22]van Trigt C. Smoothest reflectance functions I: definition and main results. *J. Opt. Soc. Am*. 1990; A 7:1891-1904.

[23]Hansen PC. *Regularization Tools: A Matlab Package for Analysis and Solution of Discrete Ill-Posed Problems*. Technical University of Denmark 1992.

[24]Hansen PC. *The truncated SVD as a method for regularization*. BIT 1987; 27: 534-553.

[25]Hansen PC. *Regularization GSVD and Truncated GSVD*. Oak Ridge National Laboratory, TM 10779. 1988

[26]Versluis R, Prowles R, Rubin M. *Optics version 5.1.01*. Lawrence Berkley National Laboratory. Retrieved 20 Nov 2007, from http://windows.lbl.gov/software.

[27]Hansen PC. Analysis of Discrete Ill-posed problems by means of the L-curve. *Society for Industrial and Applied Mathematics* 1992; 34: 561-580

[28]Hansen PC, O' Leary DP. The Use of the L-curve in the regularization of discrete ill-posed problems, *SIAM J. Sci. Comput*. 1993; 14: 1487-1503.

LIST OF FIGURES

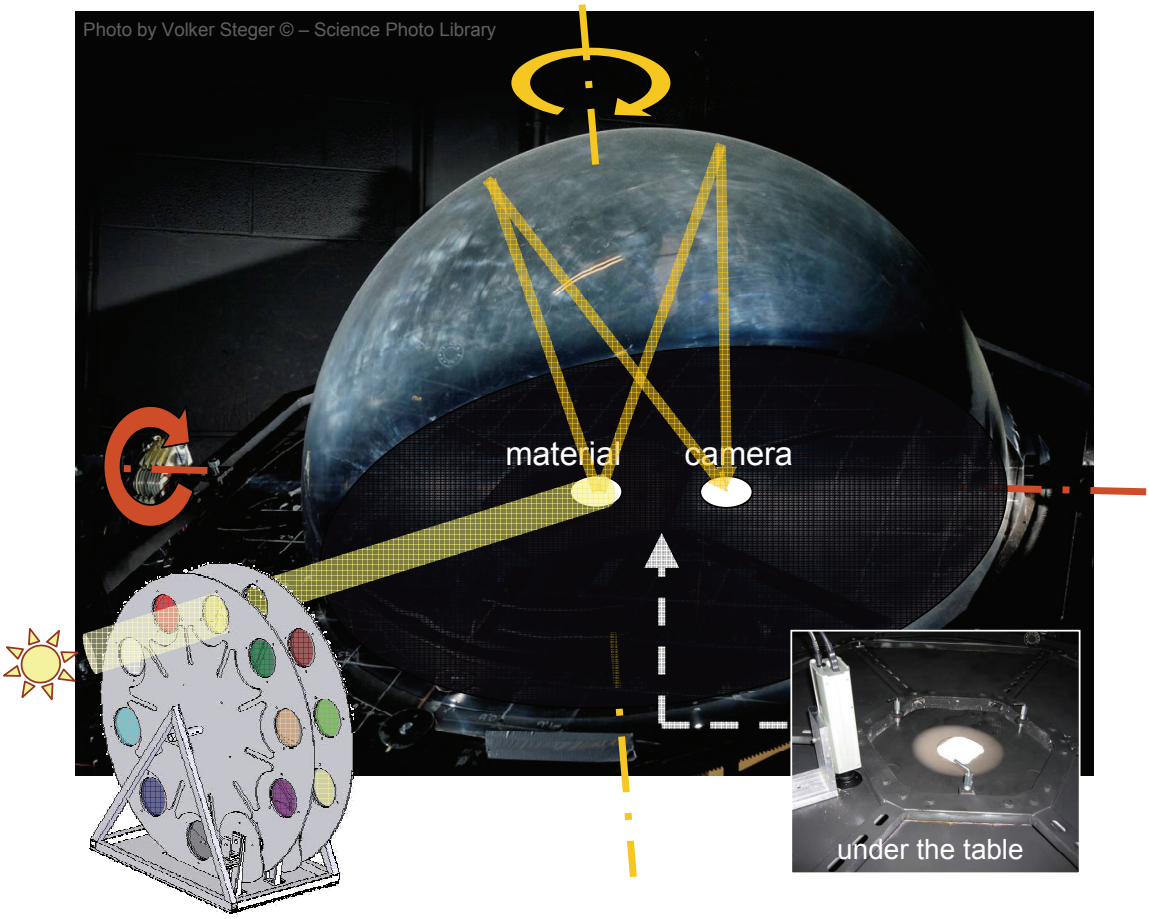
Photo by Volker Steger © – Science Photo Library
material
camera
under the table

Figure 1

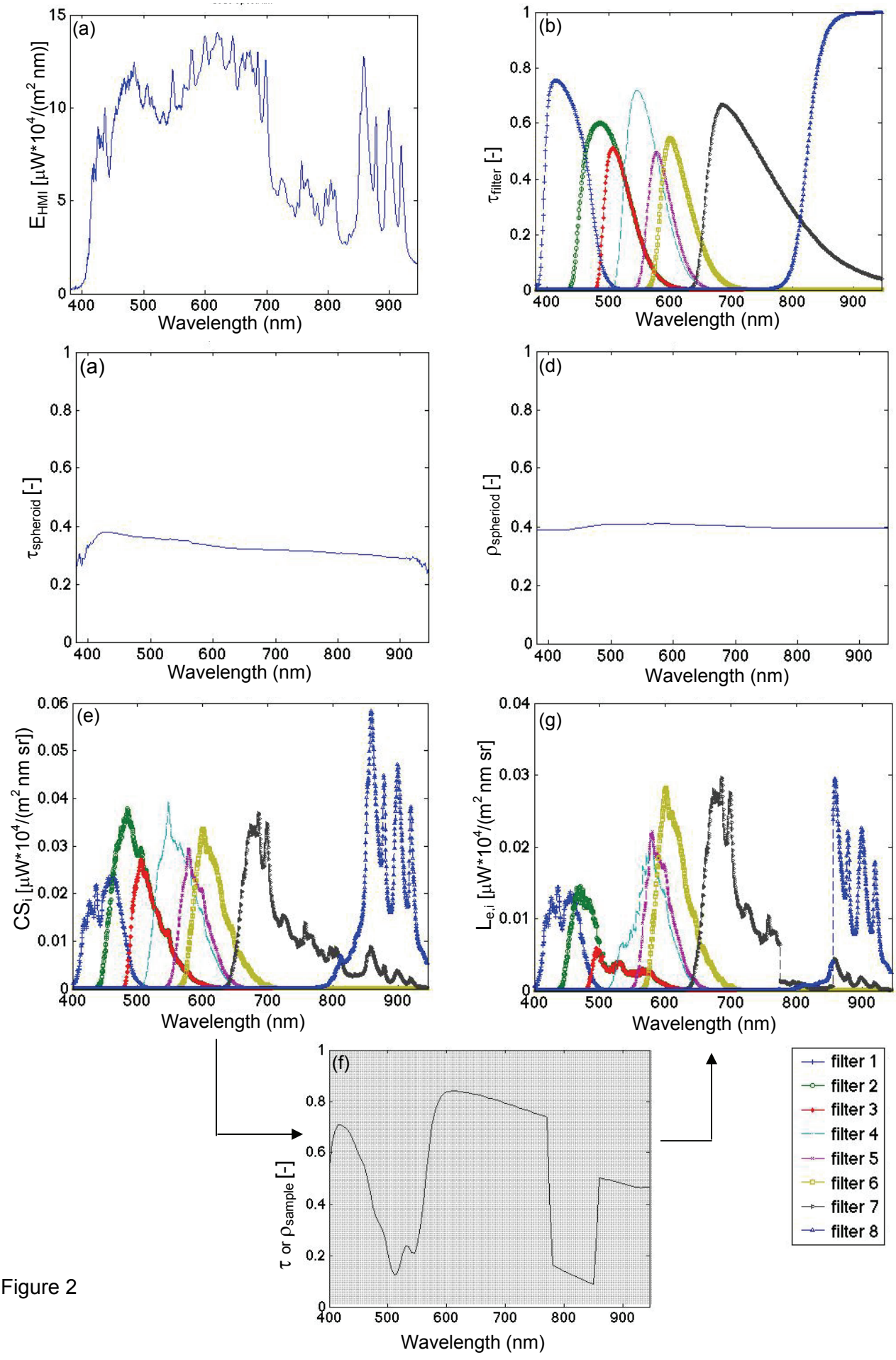
(a)
E_{HMI} [µW*10^4/(m^2 nm)]
Wavelength (nm)
(b)
τ_{filter} [-]
Wavelength (nm)
(a)
$\tau_{spheroid}$ [-]
Wavelength (nm)
(d)
$\rho_{spheriod}$ [-]
Wavelength (nm)
(e)
CS_i [µW*10^4/(m^2 nm sr)]
Wavelength (nm)
(g)
$L_{e,i}$ [µW*10^4/(m^2 nm sr]
Wavelength (nm)
(f)
τ or ρ_{sample} [-]
Wavelength (nm)
filter 1
filter 2
filter 3
filter 4
filter 5
filter 6
filter 7
filter 8

Figure 2

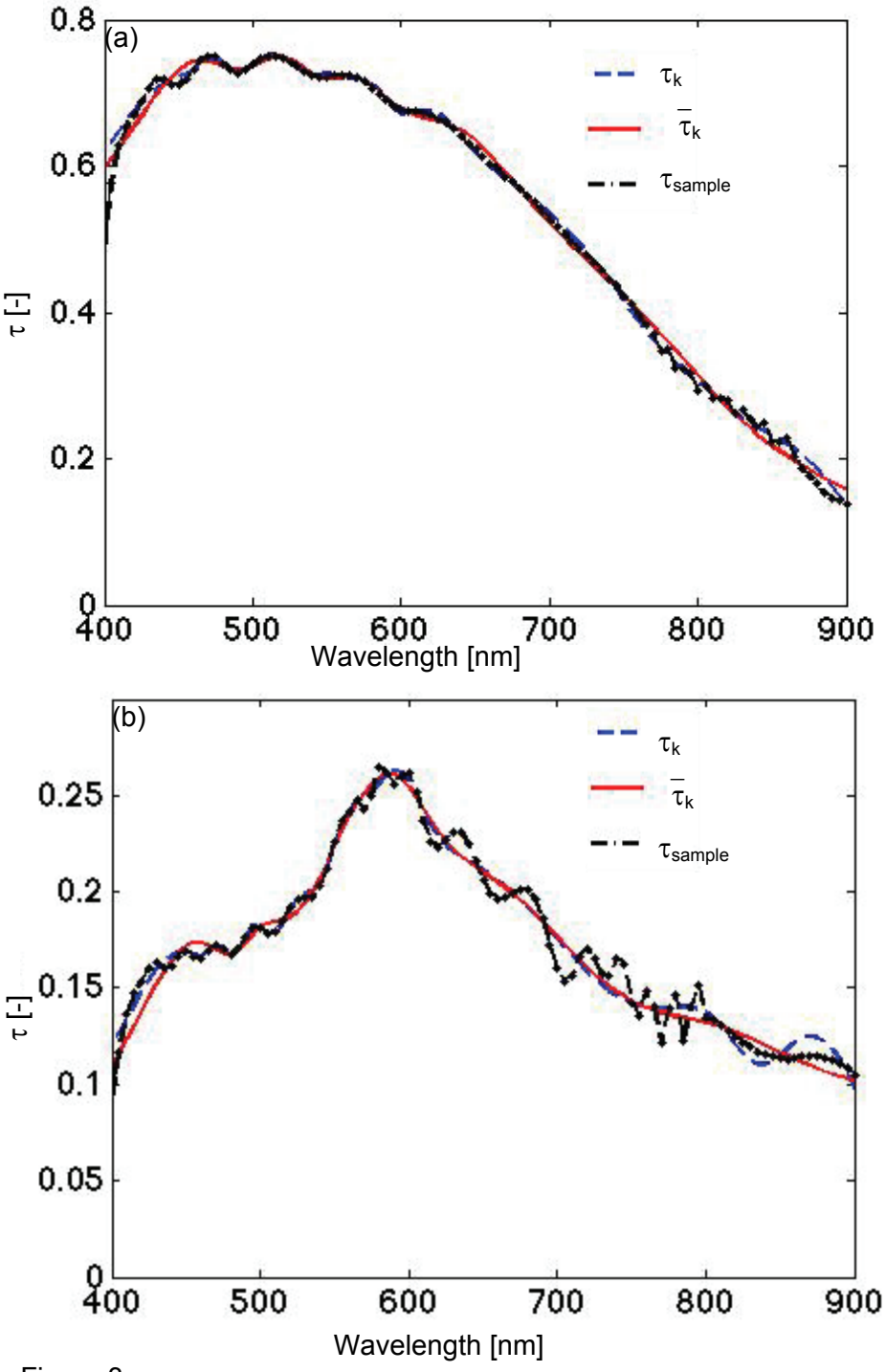
(a)
τ_k
$\bar{\tau}_k$
τ_{sample}
τ [-]
Wavelength [nm]
(b)
τ_k
$\bar{\tau}_k$
τ_{sample}
τ [-]
Wavelength [nm]

Figure 3

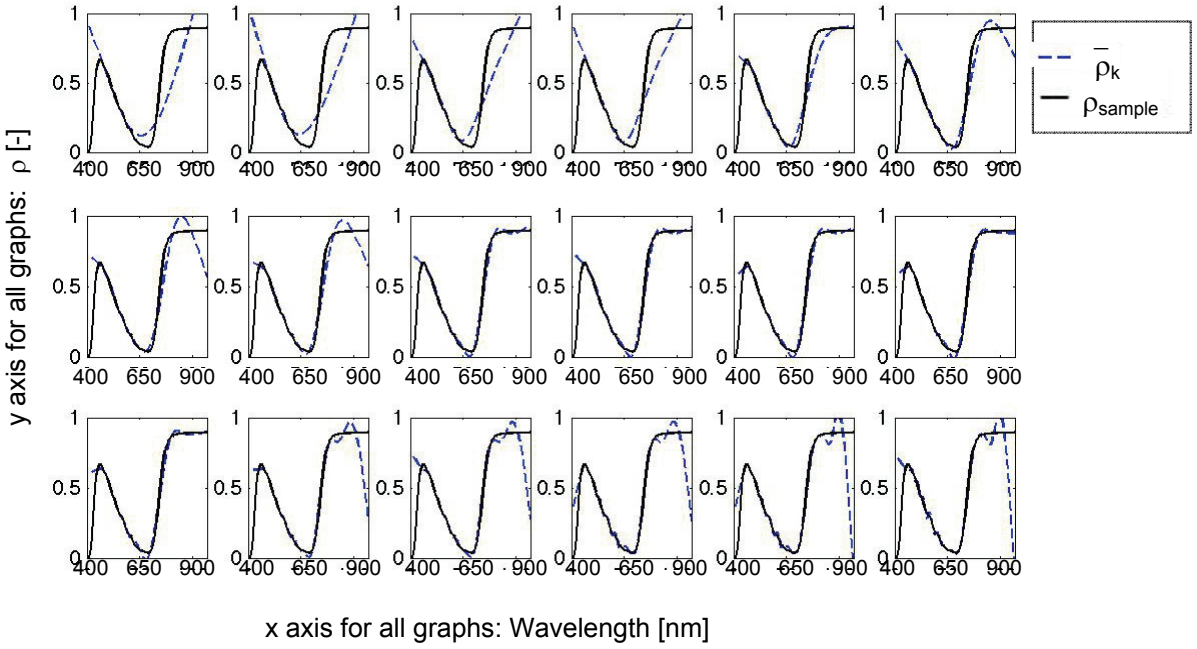
y axis for all graphs: ρ [-]
x axis for all graphs: Wavelength [nm]
$\bar{\rho}_k$
ρ_{sample}

Figure 4

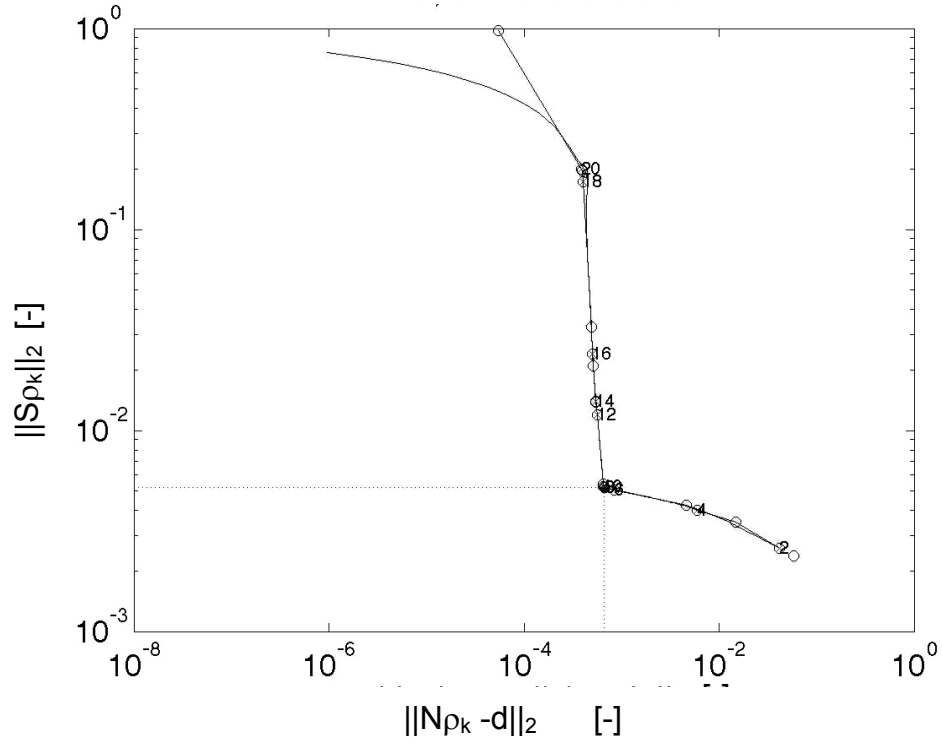
10^0
10^{-1}
10^{-2}
10^{-3}
$||S\rho_k||_2$ [-]
20
18
16
14
12
4
2
10^{-8}
10^{-6}
10^{-4}
10^{-2}
10^0
$||N\rho_k - d||_2$ [-]

Figure 5

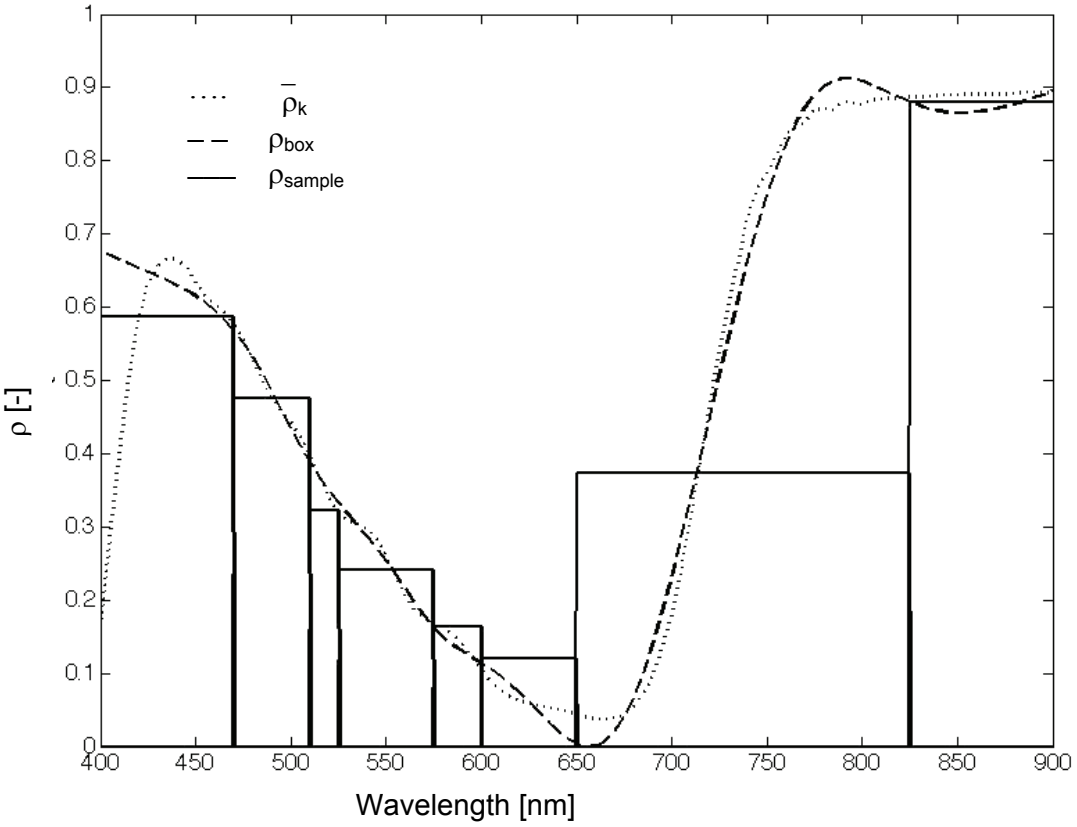
$\bar{\rho}_k$
ρ_{box}
ρ_{sample}
ρ [-]
Wavelength [nm]
0
0.1
0.2
0.3
0.4
0.5
0.6
0.7
0.8
0.9
1
400
450
500
550
600
650
700
750
800
850
900

Figure 6

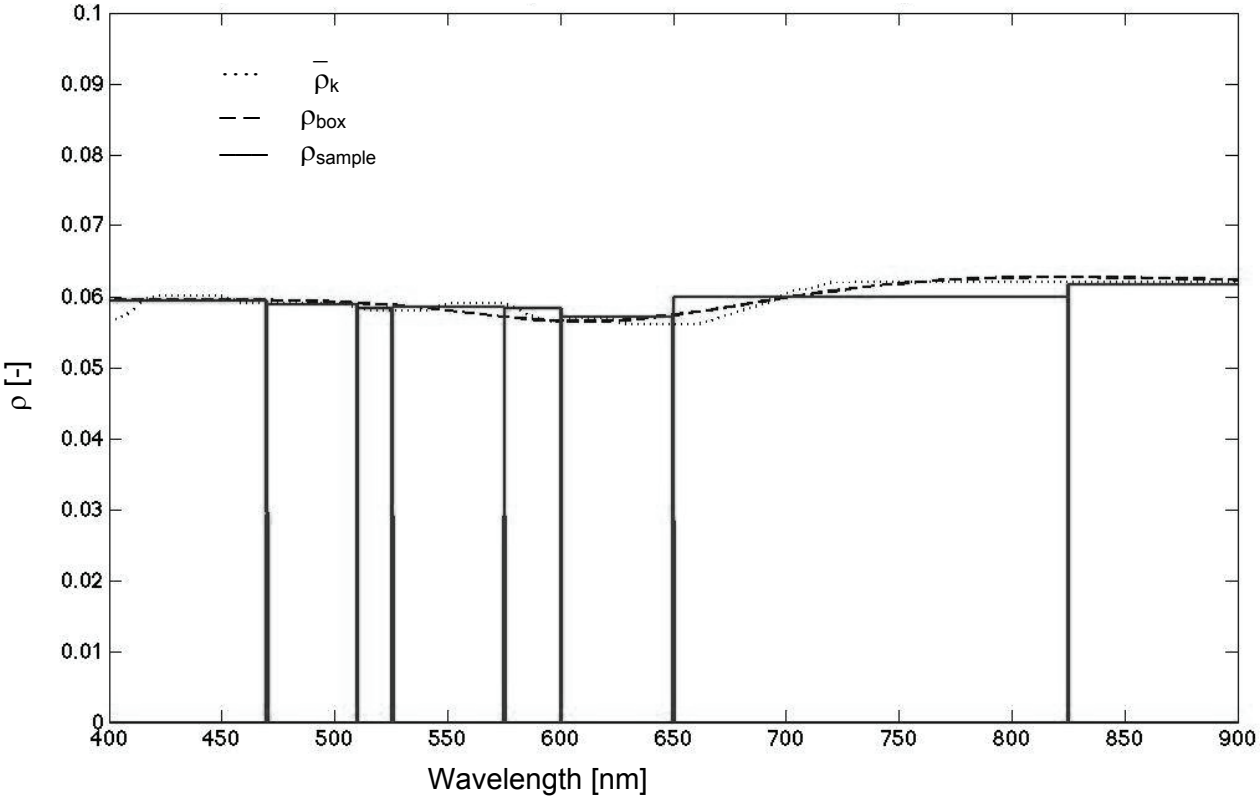
0.1
0.09
0.08
0.07
0.06
0.05
0.04
0.03
0.02
0.01
0
ρ [-]
$\bar{\rho}_k$
ρ_{box}
ρ_{sample}
400
450
500
550
600
650
700
750
800
850
900
Wavelength [nm]

Figure 7

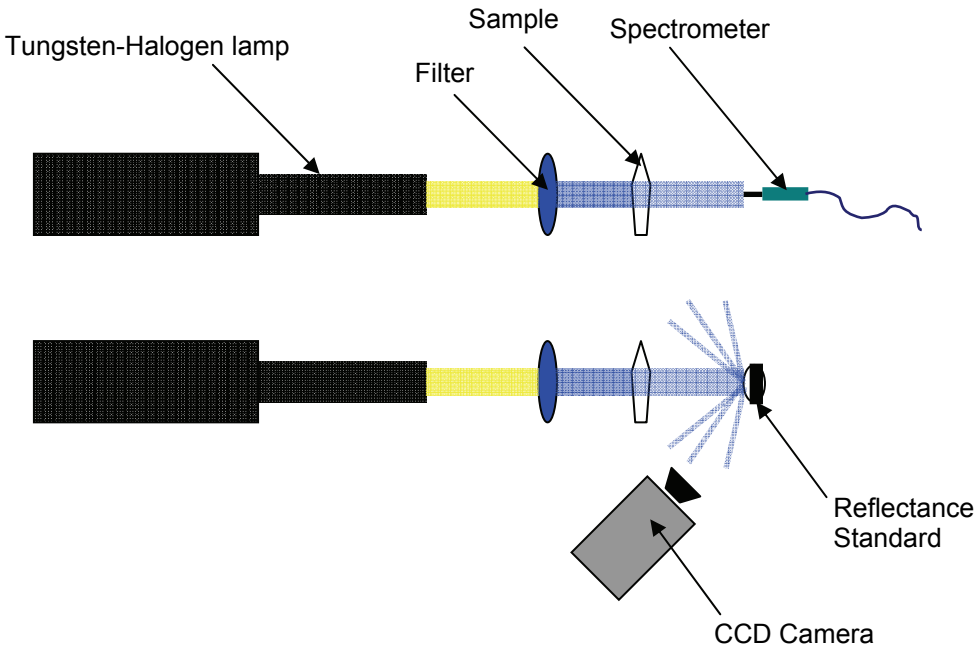
Tungsten-Halogen lamp
Sample
Spectrometer
Filter
Reflectance
Standard
CCD Camera

Figure 8

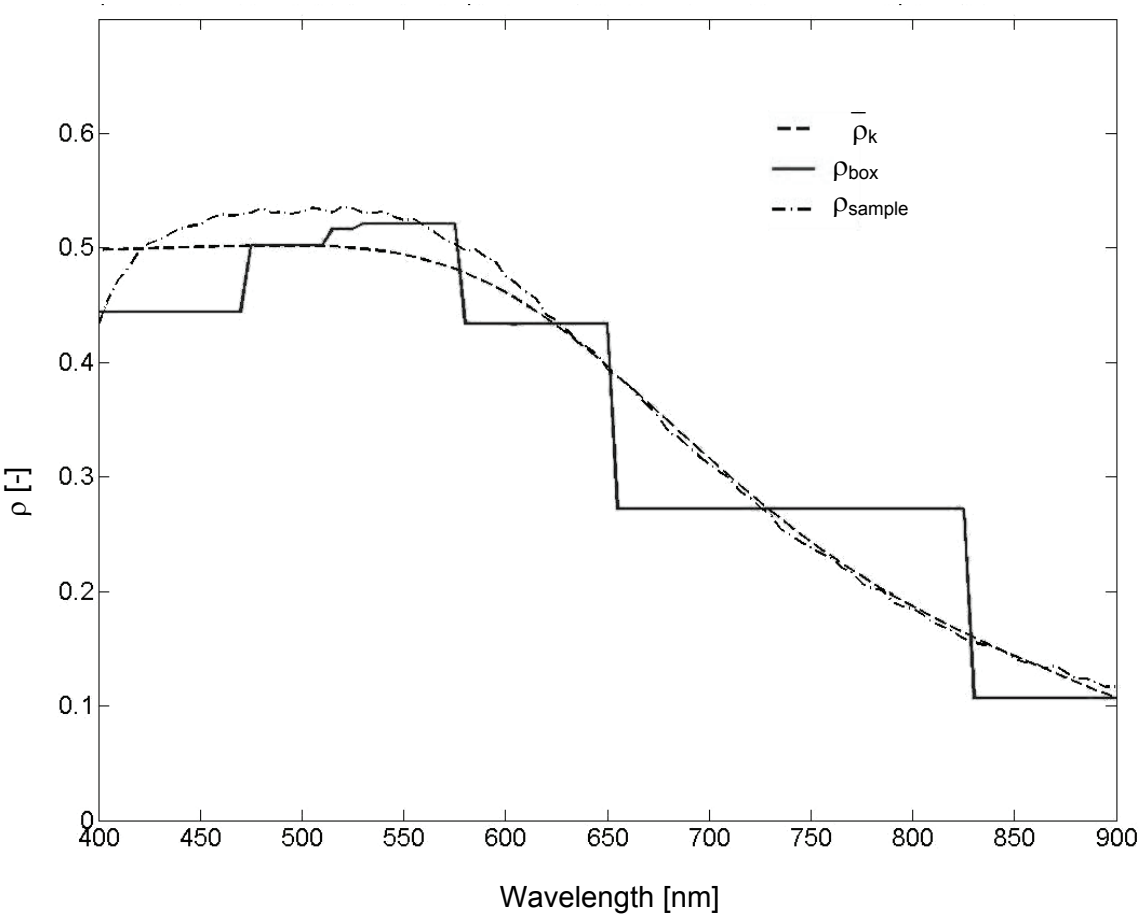
$\bar{\rho}_k$
ρ_{box}
ρ_{sample}
ρ [-]
0
0.1
0.2
0.3
0.4
0.5
0.6
400
450
500
550
600
650
700
750
800
850
900
Wavelength [nm]

Figure 9

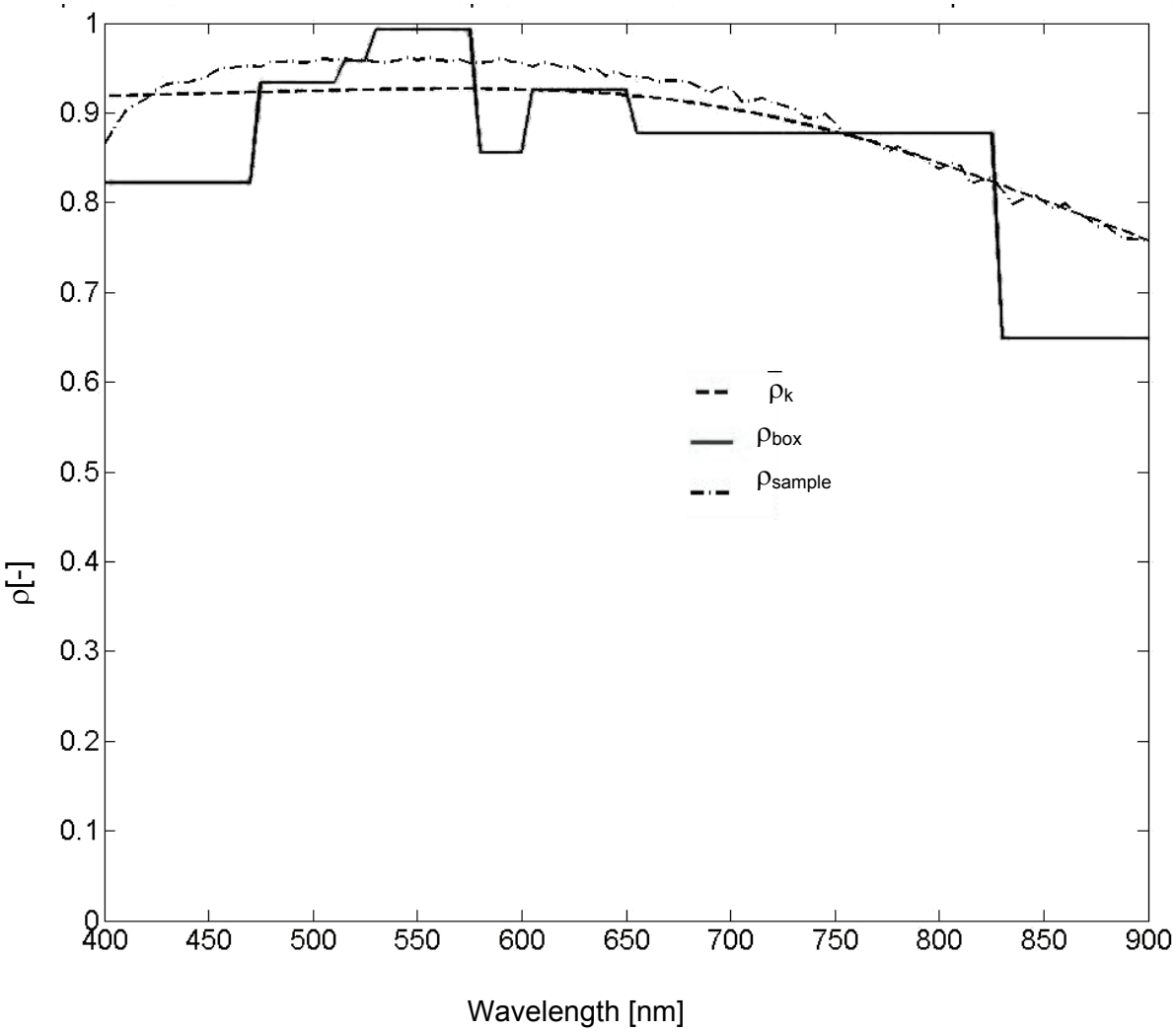
1
0.9
0.8
0.7
0.6
0.5
0.4
0.3
0.2
0.1
0
ρ[-]
400
450
500
550
600
650
700
750
800
850
900
Wavelength [nm]
$\bar{\rho}_k$
ρ_{box}
ρ_{sample}

Figure 10